Title
Constraining Dark Matter Halo Profiles and Galaxy Formation Models Using Spiral Arm Morpholohy. I. Method Outline

Permalink
https://escholarship.org/uc/item/7wr0s8x0

Journal
The Astrophysical Journal, 645

Author
Seigar, Marc S

Publication Date
2006-07-10

Peer reviewed

CONSTRAINING DARK MATTER HALO PROFILES AND GALAXY FORMATION MODELS USING SPIRAL ARM MORPHOLOGY. I. METHOD OUTLINE

MARC S. SEIGAR,[1] JAMES S. BULLOCK,[1] AARON J. BARTH,[1] AND LUIS C. HO[2]

ABSTRACT

We investigate the use of spiral arm pitch angles as a probe of disk galaxy mass profiles. We confirm our previous result that spiral arm pitch angles (P) are well correlated with the rate of shear (S) in disk galaxy rotation curves by using a much larger sample (51 galaxies) than used previously (17 galaxies). We use this correlation to argue that imaging data alone can provide a powerful probe of galactic mass distributions out to large look-back times. In contrast to previous work, we show that observed spiral arm pitch angles are similar when measured in the optical (at 0.4 μm) and the near-infrared (at 2.1 μm) with a mean difference of $2\overset{\circ}{.}3 \pm 2\overset{\circ}{.}7$. This is then used to strengthen the known correlation between P and S using B-band images. We then use two example galaxies to demonstrate how an inferred shear rate coupled with a bulge-disk decomposition model and a Tully-Fisher–derived velocity normalization can be used to place constraints on a galaxy's baryon fraction and dark matter halo profile. We show that ESO 582-G12, a galaxy with a high shear rate (slightly declining rotation curve) at $\sim$10 kpc, favors an adiabatically contracted halo, with high initial NFW concentration ($c_{\rm vir} > 16$) and a high fraction of halo baryons in the form of stars ($\sim$15%–40%). In contrast, IC 2522 has a low shear rate (rising rotation curve) at $\sim$10 kpc and favors non-adiabatically contracted models with low NFW concentrations ($c_{\rm vir} \simeq 2$–8) and a low stellar baryon fraction <10%.

Subject headings: dark matter — galaxies: fundamental parameters — galaxies: halos — galaxies: kinematics and dynamics — galaxies: spiral — galaxies: structure

1. INTRODUCTION

The correlation found between spiral arm pitch angle and rotation curve shear rate (Seigar et al. 2004, 2005) suggests that there is a link between the tightness of spiral structure and the central mass concentration in spiral galaxies. The shear rate, S, a dimensionless quantity, can be measured directly from rotation curves and is defined as

$$S = \frac{A}{\omega} = \frac{1}{2}\left(1 - \frac{R}{V}\frac{dV}{dR}\right), \qquad (1)$$

where A is the first Oort constant, ω is the angular velocity, and V is the velocity at a radius R. The shear rate depends on the shape of the rotation curve. For a rotation curve that remains flat, $S = 0.5$, for a falling rotation curve, $S > 0.5$, and for a continually rising rotation curve, $S < 0.5$. As the shape of a rotation curve depends on the mass distribution, the shear rate at any given position depends on the mass within that radius, i.e., the central mass concentration. As a result, the spiral arm pitch angle is dependent on the central mass concentration, and this is consistent with the expectations of most spiral density wave models (e.g., Bertin et al. 1989a, 1989b; Bertin 1991, 1993, 1996; Bertin & Lin 1996; Fuchs 1991, 2000), although density wave models predict that pitch angles also depend on stability (i.e., the Toomre Q-parameter).

The modal theory of spiral structure (Bertin et al. 1989a, 1989b; Bertin 1991, 1993, 1996; Bertin & Lin 1996) predicts that the tightness of the arms comes from the central mass concentration. Galaxies with higher central mass concentrations, i.e., higher overall densities (including dark matter), are predicted to have more tightly wound spiral arms. The models of Fuchs (1991, 2000) result in disks with rigidly rotating spiral modes, in which bulges act as inner reflectors of waves or modes induced by the swing amplification method, thus leading to modal spiral waves, which form as a result of Toomre swing amplification (Toomre 1981). Fuchs (2000) adopts a stellar-dynamical analog (Julian & Toomre 1966) of the Goldreich & Lynden-Bell (1965) sheet, which describes the local dynamics of an unbounded patch of thin, differentially rotating stellar disk. He then increases Q in the Goldreich & Lynden-Bell (1965) sheet, which has the effect that the bulge acts as an inner boundary. The result is that instead of shearing density waves (as in the unbounded sheet), spiral modes appear. These models best show how central mass concentration correlates with spiral arm pitch angle. If the disk is very light (low σ, where σ is the disk density) the mode can be very tight, and we are in the domain of small epicycles. Formally, if the stability parameter $Q = c\kappa/\pi G\sigma$ is close to unity, the value of c must also be small, where c is the radial velocity dispersion, and κ is the epicyclic frequency. If we increase the relative mass of the disk, we find a trend toward more open structures.

Recent observational studies of spiral structure have highlighted a difference in the morphologies seen in the optical compared with the near-infrared. The classification of galaxies by Hubble type (Hubble 1926) is performed in the optical regime, in which dust extinction still has a large effect, and where the light is dominated by the young Population I stars. In the near-infrared dust extinction is minimized, and the light is dominated by old and intermediate-age stars (Rhoads 1998; Worthey 1994). Previous work has found that optically determined Hubble type is not correlated with the near-infrared morphology. There is not a good correlation between Hubble type and near-infrared bulge-to-disk ratio or near-infrared spiral arm pitch angle (de Jong 1996; Seigar & James 1998a, 1998b). However, even in the optical regime, the correlation between quantitative pitch angle and Hubble type is weak (Kennicutt 1981), even though the tightness of the spiral arm pattern, as judged by eye, is one of the defining Hubble

[1] Department of Physics and Astronomy, 4129 Frederick Reines Hall, University of California, Irvine, CA 92697-4575.

[2] The Observatories of the Carnegie Institution of Washington, 813 Santa Barbara Street, Pasadena, CA 91101.

morphological criteria. Furthermore, it has been shown that near-infrared morphologies of some spiral galaxies can be significantly different from their optical morphologies (Block & Wainscoat 1991; Block et al. 1994; Thornley 1996; Seigar & James 1998a, 1998b; Seigar et al. 2003). Galaxies with flocculent spiral structure in the optical may present grand-design spiral structure in the near-infrared (Thornley 1996; Seigar et al. 2003). These results suggest that the optical morphology gives incomplete information about the nature of spiral structure in disk galaxies. This is the basis of the near-infrared studies of Block et al. (1999) and Seigar et al. (2005).

However, work by Eskridge et al. (2002) showed that when assigning a Hubble type to galaxies in several different wave bands, from the optical to the near-infrared, a correlation exists between the optically determined Hubble type and that determined in the near-infrared. This suggests that while there may be large small-scale differences between optical and near-infrared morphologies of spiral structure, the large-scale differences are minimal. As a result, it may be possible that there is no significant difference between the large-scale spiral arm pitch angle, regardless of whether it is determined in the optical or near-infrared for the regular "grand-design" spirals investigated here. It should be noted that for flocculent spiral structure it is difficult to determine a pitch angle for the two-armed component in the optical, while a $m = 2$ grand-design structure may be seen in the near-infrared (e.g., Thornley 1996; Grosbol & Patsis 1998; Seigar et al. 2003). As a result it may be possible to use optical imaging to expand the sample of galaxies having quantitative measurements of spiral arm pitch angle and therefore strengthen the correlation between spiral arm pitch angle and rotation curve shear rate reported by Seigar et al. (2005).

In addition to providing an important constraint on models of spiral arm formation, the correlation between spiral arm pitch angle and shear rate opens up a fundamentally new approach for probing mass distributions in spiral galaxies. This approach relies on imaging data alone, without the need for full rotation curve information. Specifically, the Tully-Fisher relation (Tully & Fisher 1977) for spiral galaxies coupled with the shear rate-pitch angle relation can be used to determine a rotation curve normalization *and* slope. In this paper we explicitly demonstrate how, given a bulge-disk decomposition, a pitch angle determination, and a Tully-Fisher normalization, one can constrain galaxy mass distributions, dark matter halo concentrations, and other galaxy formation parameters. We obtain our constraints within the context of the standard framework of disk formation put forth by Fall & Efstathiou (1980) and Blumenthal et al. (1986).

In principle, the technique we demonstrate here can be applied generally to a large sample of galaxies and to galaxies at high redshift, when spiral arms are detected. This is the first in a series of papers in which we use spiral arm pitch angles to determine the mass distribution in spiral galaxies. In this paper we determine mass concentrations in a few disk galaxies from their spiral arm pitch angles (or shear rates) and their disk masses and scale lengths (determined via a bulge-disk decomposition technique). In future papers we will apply the outline methods in this paper to a large sample of nearby disk galaxies and to a large sample of galaxies at higher redshift in order to determine the evolution in the central mass concentrations of disk galaxies as a function of look-back time.

This paper is arranged as follows. In § 2 we describe the data used and the methods for determining spiral arm pitch angles and rotation curve shear rates. In § 3 we compare pitch angles in the near-infrared and optical. In § 4 we discuss the relationship between spiral arm pitch angle and rotation curve shear rate found

by Seigar et al. (2005), and we use more data to strengthen this correlation. In § 5 we use a bulge-disk decomposition routine and an adiabatic infall model for disk galaxy formation to investigate the link between shear rate and central mass concentration, and we summarize our findings in § 6.

2. OBSERVATIONS AND DATA REDUCTION

We have made use of *H*- and *B*-band images of 57 galaxies from the Ohio State University Bright Spiral Galaxy Survey (OSUBSGS; e.g., Eskridge et al. 2002). These galaxies were chosen to be as face-on as possible (with a ratio of the minor to major axis $b/a > 0.5$) so that a comparison of spiral arm morphology could be made in the optical and near-infrared.

We also include *B*-band images of 31 galaxies that also have measured rotation curves (Mathewson et al. 1992; Persic & Salucci 1995). We observed these galaxies as part of an ongoing survey of the 600 brightest southern hemisphere galaxies. The observations make use of the CCD direct imaging camera at the 2.5 m du Pont telescope at the Las Campanas Observatory in Chile. Integration times used were 2×360 s. For this work, we selected from the full imaging data set a sample of galaxies having a ratio of the minor to major axis $b/a > 1/3$, so that spiral arm morphology can be studied, and rotation curves are also available. Of these galaxies, six also have K_s-band data. The K_s-band images were observed using the Wide-field Infrared Camera (WIRC), also at the 2.5 m du Pont telescope. A five-point dither pattern was used with integration times of 3×60 s in each position. The total exposure was therefore 900 s.

We also include *B*- and K_s-band images of a further three galaxies from our survey, which do not have rotation curves. The selection for these galaxies satisfies the same selection criteria that was used to select the OSUBSGS galaxies above.

2.1. *Measurement of Spiral Arm Pitch Angles*

Spiral arm pitch angles are measured using the same technique employed by Seigar et al. (2005). A two-dimensional fast-Fourier transform technique (FFT) is used, which employs a program described by Schröder et al. (1994). Logarithmic spirals are assumed in the decomposition. The resulting pitch angles are listed in Tables 1, 2 and 3.

The amplitude of each Fourier component is given by

$$A(m,p) = \frac{\sum_{i=1}^{I} \sum_{j=1}^{J} I_{ij}(\ln r, \theta) \exp\left[-i(m\theta + p \ln r)\right]}{\sum_{i=1}^{I} \sum_{j=1}^{J} I_{ij}(\ln r, \theta)}, \quad (2)$$

where r and θ are polar coordinates, $I(\ln r, \theta)$ is the intensity at position $(\ln r, \theta)$, m represents the number of arms or modes, and p is the variable associated with the pitch angle P, defined by $\tan P = -(m/p)$. Throughout this work we measure the pitch angle P of the $m = 2$ component. The resulting pitch angle measured using equation (2) is in radians, and this is later converted to degrees for ease of perception.

The range of radii over which the Fourier fits were applied were selected to exclude the bulge or bar (where there is no information about the arms) and to extend out to the outer limits of the arms in our images in such a way that the 10 kpc radius fell approximately in the middle of this range. The radial extent of the bar was measured manually (see, e.g., Grosbol et al. 2004), and the inner radial limit applied to the FFT was chosen to be outside this radius. Physical distances are calculated using a Hubble constant $H_0 = 75$ km s^{-1} Mpc^{-1} and recessional velocities from the NASA Extragalactic Database (NED). Pitch angles are then determined from peaks in the Fourier spectra, as this is the most

TABLE 1
B-Band and *H*-Band Spiral Arm Pitch Angles for 57 Galaxies from OSUBSGS

Galaxy Name	Hubble Type	b/a	P.A. (deg)	Radial Ranges (arcsec)	P_B (deg)	P_H (deg)
NGC 150	SBbc	0.50	118	70–126; 65–131; 75–121	8.4 ± 0.1	9.4 ± 0.8
NGC 157	SABbc	0.64	30	65–121; 60–126; 70–116	25.2 ± 0.7	25.8 ± 1.1
NGC 289	SABbc	0.71	130	40–150; 35–155; 45–145	25.7 ± 0.9	18.4 ± 2.2
NGC 578	SABc	0.63	110	65–125; 60–130; 70–120	18.0 ± 0.2	18.8 ± 0.5
NGC 613	SBbc	0.76	120	73–135; 68–140; 78–130	26.4 ± 1.0	41.8 ± 1.8
NGC 864	SABc	0.74	20	55–143; 50–148; 60–138	46.4 ± 1.3	42.9 ± 3.0
NGC 1073	SBc	0.92	15	73–183; 68–188; 78–178	17.6 ± 0.8	11.9 ± 0.8
NGC 1087	SABc	0.59	5	57–147; 52–152; 62–142	31.1 ± 1.6	32.7 ± 0.5
NGC 1187	SBc	0.75	130	90–132; 85–137; 95–127	15.7 ± 0.9	15.1 ± 1.5
NGC 1241	SBb	0.61	140	25–51; 20–56; 30–46	50.3 ± 1.4	44.2 ± 3.0
NGC 1300	SBbc	0.66	106	80–116; 75–121; 85–111	31.7 ± 1.1	29.0 ± 1.4
NGC 1350	SBab	0.54	0	75–87; 72–90; 78–84	48.8 ± 4.8	52.0 ± 3.8
NGC 1792	SABc	0.50	137	45–211; 40–216; 50–206	42.1 ± 4.3	47.0 ± 1.8
NGC 2090	SAb	0.50	13	64–272; 59–277; 69–267	20.3 ± 0.3	20.3 ± 0.8
NGC 2139	SABcd	0.73	140	50–118; 45–123; 55–113	26.4 ± 3.3	30.2 ± 1.9
NGC 2964	SABbc	0.55	97	70–162; 65–167; 75–157	46.9 ± 3.9	47.5 ± 2.5
NGC 3223	SAbc	0.61	135	32–74; 27–79; 37–69	10.7 ± 2.0	7.1 ± 1.4
NGC 3261	SBbc	0.76	85	30–90; 25–95; 35–86	21.2 ± 1.7	22.4 ± 1.1
NGC 3338	SAc	0.61	100	74–164; 69–169; 79–159	13.6 ± 0.3	16.2 ± 0.6
NGC 3507	SBb	0.85	110	120–196; 115–201; 125–191	24.0 ± 2.4	23.2 ± 2.0
NGC 3513	SBc	0.79	75	80–130; 75–135; 85–125	28.1 ± 4.3	25.2 ± 2.9
NGC 3583	SBb	0.64	125	60–84; 57–87; 63–81	32.5 ± 2.6	36.9 ± 1.9
NGC 3646	SABc	0.56	50	20–52; 15–57; 25–47	21.7 ± 3.0	17.0 ± 2.3
NGC 3686	SBbc	0.78	15	99–169; 94–174; 104–164	15.3 ± 4.2	13.4 ± 2.8
NGC 3726	SABc	0.69	10	100–258; 95–263; 105–253	32.0 ± 4.4	31.7 ± 1.2
NGC 3810	SAc	0.70	15	112–200; 107–205; 117–195	31.0 ± 2.8	30.4 ± 4.3
NGC 3887	SBbc	0.76	20	93–163; 88–168; 98–158	24.9 ± 3.9	24.4 ± 2.6
NGC 3893	SABc	0.62	165	102–218; 97–223; 107–213	18.2 ± 0.5	19.5 ± 0.5
NGC 4027	SBdm	0.75	167	60–126; 55–131; 65–121	35.7 ± 5.0	37.6 ± 3.2
NGC 4030	SAbc	0.71	27	51–161; 46–166; 56–156	19.8 ± 3.2	20.6 ± 3.5
NGC 4051	SABbc	0.75	135	185–257; 180–262; 190–267	18.3 ± 3.6	17.7 ± 1.7
NGC 4145	SABd	0.73	100	93–211; 88–216; 98–206	43.3 ± 2.9	43.6 ± 2.7
NGC 4414	SAc	0.56	155	142–290; 137–295; 147–285	13.2 ± 2.6	7.7 ± 1.8
NGC 4548	SBb	0.80	150	250–386; 245–391; 255–381	24.8 ± 0.4	31.0 ± 0.6
NGC 4580	SABa	0.76	165	82–218; 77–223; 87–213	22.1 ± 4.8	22.1 ± 2.4
NGC 4654	SABcd	0.57	128	99–199; 94–204; 104–194	32.1 ± 2.6	30.4 ± 1.4
NGC 4930	SBbc	0.82	40	43–77; 38–82; 48–72	40.4 ± 4.2	41.2 ± 3.9
NGC 4939	SAbc	0.51	10	24–76; 19–81; 29–71	22.4 ± 1.8	22.3 ± 1.7
NGC 4995	SABb	0.64	95	31–145; 26–150; 36–140	17.8 ± 0.7	18.0 ± 0.5
NGC 5054	SAbc	0.59	160	51–127; 46–132; 56–122	49.3 ± 3.4	47.7 ± 2.7
NGC 5085	SAc	0.88	38	20–138; 15–143; 25–133	16.3 ± 2.8	16.9 ± 1.3
NGC 5247	SAbc	0.88	20	47–181; 42–186; 52–176	49.5 ± 0.7	46.3 ± 0.5
NGC 5371	SABbc	0.80	8	42–78; 37–83; 47–73	38.7 ± 1.2	37.1 ± 0.9
NGC 5483	SBc	0.92	25	50–124; 55–119; 45–129	29.6 ± 1.3	31.0 ± 1.2
NGC 5921	SBbc	0.82	130	70–140; 65–145; 75–135	25.1 ± 1.0	26.6 ± 0.8
NGC 6215	SAc	0.86	78	47–141; 42–146; 52–136	36.7 ± 4.0	34.3 ± 3.6
NGC 6221	SBbc	0.71	5	73–135; 68–140; 78–130	40.4 ± 3.2	32.8 ± 1.3
NGC 6300	SBb	0.67	118	99–179; 94–184; 104–174	26.2 ± 2.9	26.4 ± 1.1
NGC 6384	SABbc	0.66	30	60–126; 55–131; 65–121	17.8 ± 1.2	17.0 ± 0.8
NGC 6907	SBbc	0.82	46	40–58; 38–60; 42–56	20.3 ± 0.7	24.7 ± 0.5
NGC 7083	SABc	0.59	5	32–78; 29–81; 35–75	24.9 ± 0.9	25.7 ± 0.5
NGC 7412	SABc	0.74	65	50–90; 45–95; 55–85	29.4 ± 2.2	28.6 ± 1.7
NGC 7418	SABcd	0.74	139	63–151; 58–156; 68–146	22.3 ± 3.7	23.3 ± 2.2
NGC 7479	SBc	0.76	25	48–82; 45–85; 51–79	17.8 ± 1.2	17.5 ± 0.9
NGC 7552	SBab	0.79	1	63–133; 58–138; 68–128	19.3 ± 1.7	19.9 ± 1.1
NGC 7723	SBb	0.66	40	72–104; 67–109; 77–99	16.1 ± 2.5	15.3 ± 2.0
NGC 7741	SBcd	0.68	170	165–247; 160–252; 170–242	28.5 ± 2.6	30.1 ± 2.1

Notes.—Col. (1) galaxy names; col. (2) optical Hubble type from de Vaucouleurs et al. (1991; hereafter RC3); col. (3) ratio of the minor to major axis, b/a from NED; col. (4) position angle from RC3; col. (5) three radial ranges used for the FFT analysis; col. (6) *B*-band pitch angle, P_B; col. (7) *H*-band pitch angle, P_H.

TABLE 2
B-Band and K_s-Band Spiral Arm Pitch Angles for Nine Galaxies from Our Survey

Galaxy Name	Hubble Type	b/a	P.A. (deg)	Radial Ranges (arcsec)	P_B (deg)	P_K (deg)
IC 2522	SAcd	0.71	0	25–77; 20–82; 30–72	38.8 ± 1.6	46.3 ± 1.2
NGC 1964......................	SABb	0.38	32	21–175; 16–180; 26–170	13.8 ± 0.2	13.0 ± 0.7
NGC 2082......................	SABc	0.94	60	50–130; 45–135; 55–125	27.6 ± 0.5	20.9 ± 0.6
NGC 2280......................	SAcd	0.49	163	55–117; 50–122; 60–112	24.2 ± 1.7	22.4 ± 2.0
NGC 2417......................	SABbc	0.68	81	25–71; 20–76; 30–66	24.0 ± 0.7	22.2 ± 3.7
NGC 2935......................	SABb	0.78	0	43–93; 38–98; 48–88	14.1 ± 0.2	16.5 ± 1.1
NGC 3318......................	SABb	0.54	78	23–89; 18–94; 28–84	36.9 ± 6.5	36.9 ± 2.2
NGC 3450......................	SBb	0.88	140	28–48; 25–51; 31–45	9.1 ± 0.4	14.5 ± 0.3
NGC 4050......................	SBab	0.68	85	70–91; 67–94; 73–88	8.9 ± 0.7	8.8 ± 1.6

Notes.—Col. (1) galaxy names; col. (2) optical Hubble type from RC3; col. (3) ratio of the minor to major axis, b/a from NED; col. (4) position angle from RC3; col. (5) three radial ranges used for the FFT analysis; col. (6) B-band pitch angle, P_B; col. (7) K_s-band pitch angle, P_K.

powerful method for finding periodicity in a distribution (Considère & Athanassoula 1988; Garcia-Gomez & Athanassoula 1993). The radial range over which the Fourier analysis was performed was chosen by eye and is probably the dominant source of error in the calculation of pitch angles, as spiral arms are only approximately logarithmic and sometimes abrupt changes can be seen in spiral arm pitch angles (e.g., Seigar & James 1998b). As a result, three radial ranges were chosen for each galaxy, and a mean pitch angle and standard error calculated for every object.

The images were first projected to face-on. Mean uncertainties of position angle and inclination as a function of inclination were discussed by Considère & Athanassoula (1988). For a galaxy with low inclination, there are clearly greater uncertainties in assigning both a position angle and an accurate inclination. These uncertainties are discussed by Block et al. (1999) and Seigar et al. (2005), who take a galaxy with low inclination ($<30°$) and one with high inclination ($>60°$) and varied the inclination angle used in the correction to face-on. They found that for the galaxy with

TABLE 3
Pitch Angles and Shear Rates for 31 Galaxies from Our Survey

Galaxy Name	Hubble Type	b/a	P.A. (deg)	Radial Ranges (arcsec)	Pitch Angle (deg)	Shear Rate
ESO 9-G10	SAc	0.76	171	27–101; 22–106; 32–96	23.7 ± 1.1	0.44 ± 0.06
ESO 121-G26	SBc	0.63	115	51–85; 46–90; 56–80	10.5 ± 0.2	0.75 ± 0.04
ESO 582-G12	SAc	0.64	48	32–102; 27–107; 37–97	22.6 ± 0.6	0.52 ± 0.05
IC 2522	SAcd	0.71	0	25–77; 20–82; 30–72	38.8 ± 1.6	0.39 ± 0.01
IC 2537	SABc	0.65	26	30–82; 25–87; 35–77	9.3 ± 0.3	0.63 ± 0.02
IC 3253	SAc	0.39	23	22–92; 17–97; 27–87	24.6 ± 2.0	0.36 ± 0.03
IC 4538	SABc	0.77	50	42–66; 37–71; 47–61	38.3 ± 3.8	0.35 ± 0.02
IC 4808	SAc	0.42	45	15–45; 10–50; 20–40	14.1 ± 0.4	0.65 ± 0.02
NGC 150........................	SBbc	0.50	118	70–126; 65–131; 75–121	8.4 ± 0.1	0.65 ± 0.03
NGC 151........................	SBbc	0.42	75	30–52; 27–55; 33–49	36.1 ± 1.5	0.52 ± 0.02
NGC 578........................	SABc	0.63	110	65–125; 60–130; 70–120	18.0 ± 0.2	0.64 ± 0.06
NGC 908........................	SAc	0.43	75	56–150; 51–155; 61–145	12.9 ± 0.4	0.59 ± 0.04
NGC 1232......................	SABc	0.88	108	53–141; 48–146; 58–136	19.3 ± 2.0	0.66 ± 0.06
NGC 1292......................	SAc	0.43	7	53–173; 48–178; 58–168	29.8 ± 1.0	0.48 ± 0.04
NGC 1300......................	SBbc	0.66	106	80–116; 75–121; 85–111	31.7 ± 1.1	0.50 ± 0.03
NGC 1353......................	SAbc	0.41	138	63–139; 58–144; 68–134	36.6 ± 1.0	0.34 ± 0.05
NGC 1365......................	SBb	0.55	32	61–129; 56–134; 66–124	35.4 ± 1.7	0.53 ± 0.03
NGC 1559......................	SBcd	0.57	64	82–156; 77–161; 87–151	20.4 ± 0.4	0.68 ± 0.06
NGC 1566......................	SABbc	0.80	60	73–133; 68–138; 78–128	36.0 ± 0.3	0.50 ± 0.04
NGC 1964......................	SABb	0.38	32	21–175; 16–180; 26–170	13.8 ± 0.2	0.61 ± 0.02
NGC 2280......................	SAcd	0.50	163	55–117; 50–122; 60–112	24.2 ± 1.7	0.32 ± 0.05
NGC 2417......................	SABbc	0.68	81	25–71; 20–76; 30–66	24.0 ± 0.7	0.63 ± 0.03
NGC 2835......................	SABc	0.67	8	110–240; 105–245; 115–235	19.5 ± 0.7	0.62 ± 0.06
NGC 2935......................	SABb	0.78	0	43–93; 38–98; 48–88	14.1 ± 0.2	0.73 ± 0.03
NGC 3052......................	SABc	0.65	102	25–57; 20–62; 30–52	19.8 ± 0.7	0.63 ± 0.02
NGC 3054......................	SABbc	0.61	118	44–84; 39–89; 49–79	42.9 ± 3.9	0.37 ± 0.02
NGC 3223......................	SAbc	0.61	135	32–74; 27–79; 37–69	10.7 ± 2.0	0.72 ± 0.02
NGC 3318......................	SABb	0.54	78	23–89; 18–94; 28–84	36.9 ± 6.5	0.53 ± 0.03
NGC 5967......................	SABc	0.59	90	46–76; 41–81; 51–71	47.3 ± 0.5	0.27 ± 0.02
NGC 7083......................	SABc	0.59	5	32–78; 29–81; 35–75	26.7 ± 1.4	0.40 ± 0.04
NGC 7392......................	SBab	0.62	123	30–66; 25–71; 35–61	24.6 ± 2.0	0.54 ± 0.02

Notes.—Col. (1) galaxy names; col. (2) Hubble types from RC3; col. (3) ratio of the minor to major axis from NED; col. (4) position angle from RC3; col. (5) three radial ranges used for the FFT analysis; col. (6) pitch angle; col. (7) shear rate.

low inclination, the measured pitch angle remained the same. However, the measured pitch angle for the galaxy with high inclination varied by $\pm 10\%$. Since inclination corrections are likely to be largest for galaxies with the highest inclinations, cases in which inclination is $>60°$ are taken as the worst case scenario. For galaxies with inclination $i > 60°$, we take into account this uncertainty. Our deprojection method assumes that spiral galaxy disks are intrinsically circular and flat in nature.

2.2. *Measurement of Shear Rates*

31 of the galaxies observed here have Hα rotation curve data measured by Mathewson et al. (1992) and Persic & Salucci (1995). These rotation curves are of good quality with an rms error <10 km s^{-1}, and an error associated with folding the two sides of the galaxy also <10 km s^{-1}. These rotation curves have been used to estimate the shear rates in these galaxies, using the same method used by other authors (e.g., Block et al. 1999; Seigar et al. 2005; Seigar 2005).

Using equation (1), we have calculated the shear rates for these galaxies, over the same radial ranges for which the Fourier analysis was performed and pitch angles calculated. We have selected several different radial ranges, just as in the Fourier analysis, and we present mean shear rates and standard errors. The dominant sources of error on the shear rate are the rms error in the rotation curve and the error associated with folding the two sides of the galaxy. This is typically $<10\%$. In order to calculate the shear rate, the mean value of dV/dR, measured in km s^{-1} arcsec^{-1}, is calculated by fitting a line of constant gradient to the outer part of the rotation curve (i.e., past the radius of turnover and any bar or bulge that may exist in the galaxy). Mean shear rates are then calculated from shear rates measured over three radial ranges, corresponding to the same radial ranges over which the Fourier analysis was performed. The resulting shear rates are listed in Table 3.

The choice of using 10 kpc as the radius at which to measure the shear and spiral arm pitch angle is somewhat arbitrary. The correlation between these two quantities (Seigar et al. 2005 and Fig. 3) only exists when they are measured at a physical radius, chosen independently of the disk scale length. If we measure pitch angles and shear at a radius chosen using the disk scale length, the correlation no longer exists, and the range of shear is narrower (between 0.4 and 0.6). As a result, we chose to measure shear and pitch angles at a radius independent of the disk scale length. We chose 10 kpc (although it could just as easily be 8 kpc or 12 kpc).

The fact that this correlation only exists for a physical radius suggests that other quantities may be important in the determination of shear and pitch angle (e.g., the disk scale length itself or the stability of the disk as a function of radius). Indeed, when modeling galaxies we use a one-dimensional bulge-disk decomposition and use the derived disk scale length in our codes.

3. A COMPARISON OF OPTICAL AND NEAR-INFRARED PITCH ANGLES

Figure 1 shows of plot of *B*-band pitch angle versus near-infrared pitch angle for the 57 face-on and nearly face-on galaxies taken from OSUBSGS and 9 face-on and nearly face-on galaxies taken from our survey. This plot shows a very tight 1:1 correlation between the optical and near-infrared spiral arm pitch angles (correlation coefficient 0.95; significance >99.99%), showing that pitch angles are similar whether measured in the optical or near-infrared regimes. In this plot, only one galaxy has a pitch angle that shows a difference of $>10°$ when measured at *B* com-
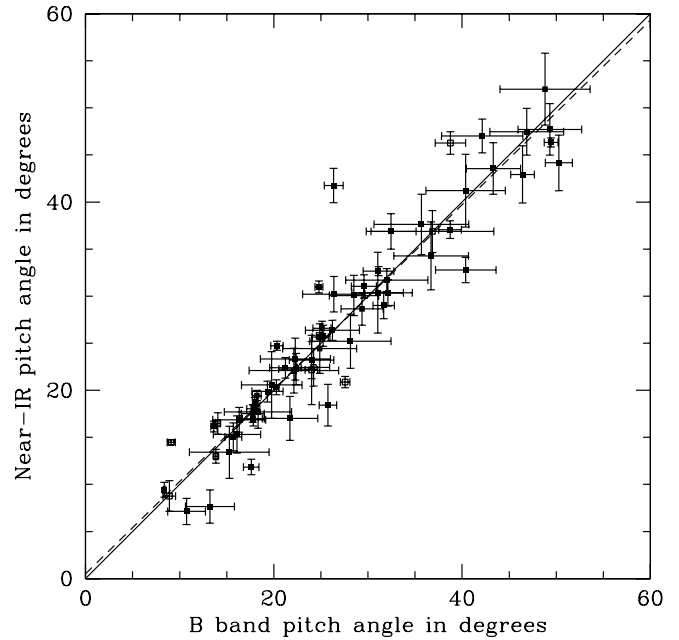

FIG. 1.—A 1:1 correlation between optical spiral arm pitch angle as measured in the *B* band and near-infrared spiral arm pitch angle as measured in the *H* band for OSUBSGS galaxies and the K_s band for our galaxies. This correlation shows that pitch angles are similar whether measured in the near-infrared or optical regime. Only one object shows a difference of $>10°$. The filled squares represent galaxies from the OSUBSGS, and the open squares represent galaxies from our survey. The solid line represents where a 1:1 correlation lies. The dashed line is the best-fit line to the data.

pared with its near-infrared measurement. The outlying galaxy is NGC 613, which appears to have a strong four-armed component in the optical, whereas this is a much weaker feature in the near-infrared. This result is in contrast to the claims of Block et al. (1999) and Block & Puerari (1999), who argue that there is usually a large difference between the spiral arm pitch angle when measured in the optical and the near-infrared. Our result is consistent with the result that Hubble types assigned to galaxies in the optical and the near-infrared correlate well with each other (Eskridge et al. 2002).

We now analyze the absolute difference between the pitch angles measured in the *B* band and those measured in the near-infrared. The distribution of this absolute difference in pitch angles is shown in Figure 2. The mean of this difference in pitch angles is $2°.3 \pm 2°.7$, where the error is a standard deviation, and this is therefore consistent with the same pitch angle being measured, regardless of the wave band. The mode of the distribution is in the range 0.5–1.0, and the median is 1.46. Furthermore, a linear fit to the data in Figure 1 yields the relationship

$$P_{\mathrm{NIR}} = (0.50 \pm 1.25) + (0.98 \pm 0.04)P_{\mathrm{opt}}, \qquad (3)$$

where P_{NIR} is the pitch angle measured in the near-infrared and P_{opt} is the pitch angle measured in the optical. The point at which this line of best fit intersects the P_{NIR}-axis is consistent with zero, and the gradient of the line is consistent with unity, and so the line of best fit is consistent with a 1:1 correlation between spiral arm pitch angles in the optical and near-infrared. It should be noted that although the difference between optical and near-infrared spiral arm pitch angles is consistent with zero from a statistical analysis, minor systematic differences cannot be excluded. Small differences between optical and near-infrared pitch angles have been measured of $1°–2°$ (e.g., Grosbol & Patsis 1998). Furthermore,
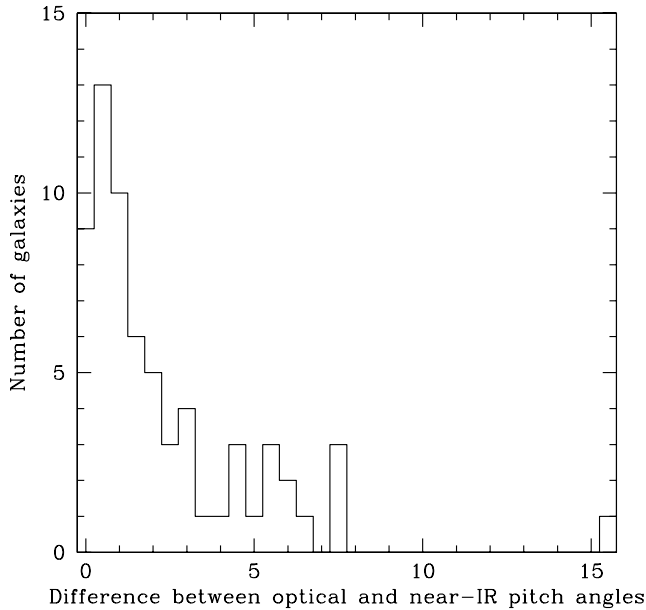
FIG. 2.—Histogram showing the distribution in the absolute difference measured between the *B*-band and *H*-band pitch angles.
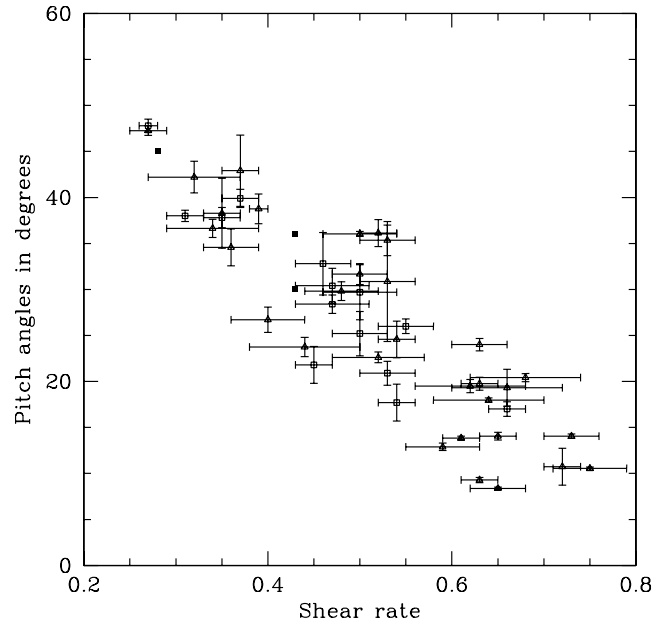

FIG. 3.—Spiral arm pitch angle vs. rotation curve shear rate, showing a strong correlation. The filled squares represent galaxies with data measured by Block et al. (1999), the open squares are galaxies from Seigar et al. (2005), and the open triangles represent the data from the present sample.

color gradients across arms may be caused by such small differences in pitch angles (e.g., Gonzalez & Graham 1996).

Of course, it is still a well-known fact that spiral structure measured in the near-infrared appears much smoother than that measured in the optical (e.g., Block & Wainscoat 1991; Block et al. 1994; Thornley 1996; Seigar et al. 2003). Even in galaxies that appear grand-design in the optical, small spokes and bifurcations are clearly seen along the length of the dominant arms. These spokes and bifurcations all but disappear in the near-infrared. However, our result suggests that the pitch angle of the large-scale spiral structure remains constant with wavelength in the range $0.4 < \lambda < 2.2\ \mu$m for spirals with a relatively strong two-armed pattern in the optical. For weaker, more flocculent galaxies there may well be significant differences due to dust. This has serious implications for the physical meaning of the dust-penetrated classification scheme (Block & Puerari 1999; Block et al. 1999). These implications are discussed in § 4.

4. THE RELATIONSHIP BETWEEN SHEAR RATE AND PITCH ANGLE

The correlation between spiral arm pitch angle and rotation curve shear rate presented by Seigar et al. (2005) only had 17 data points, including 3 from an earlier study by Block et al. (1999). Here we include a further 31 galaxies with measure pitch angles and shear rates. Figure 3 shows a plot of shear rate versus spiral arm pitch angle. A very good correlation still exists (correlation coefficient 0.89; significance 99.75%).

The shape of a rotation curve, beyond the turnover radius, is determined by the amount and distribution of matter contained in a galaxy. The increase of shear rates from low to high dictates a change in mass distributions from small to large central mass concentrations. The correlation with pitch angle is therefore interpreted as follows; galaxies with higher rates of shear present a larger central mass concentration and more tightly wound arms. In contrast, open arm morphologies are associated with lower rates of galactic shear and lower central mass concentrations. This correlation was alluded to by the pioneering work of Lin & Shu (1964) and by the later spectroscopic study of Burstein & Rubin (1985). It is in agreement with modal theories of spiral structure

(e.g., Bertin et al. 1989a, 1989b; Bertin & Lin 1996) and other numerical models based on the modal theory (e.g., Fuchs 1991, 2000).

The correlations shown in Figures 1 and 3 have significant implications for the dust-penetrated classification scheme introduced by Block & Puerari (1999). These authors argue that their dust-penetrated classification scheme is needed, because spiral arm pitch angles are different in the near-infrared when compared to the optical, and as a result they classify galaxies into three bins, based on their pitch angles when measured in the near-infrared. However, we have shown (in Fig. 1) that spiral galaxies with a relatively strong two-armed spiral pattern, have optical and near-infrared pitch angles that are nearly always very similar. This, therefore, seems to lessen the need for the dust-penetrated classification scheme. In Figure 3, however, we show that a correlation still exists between shear rate and spiral arm pitch angle, no matter which wave band the pitch angle is measured in. This suggests that classifying galaxies based on their pitch angles has some physical basis, because it tells us something about their central mass concentrations.

Given the correlation between shear rate and pitch angle, we derive the following expression relating these terms,

$$P = (64.25 \pm 2.87) - (73.24 \pm 5.53)S, \qquad (4)$$

where P is the pitch angle in degrees and S is the shear rate.

5. CONNECTING PITCH ANGLES TO CENTRAL MASS CONCENTRATIONS

Our goal now is to demonstrate how spiral arm pitch angle measurements coupled with a bulge-disk decomposition can be used to constrain the overall mass distribution in spiral galaxies. We outline the method for two example galaxies with pseudo-bulges (see Kormendy & Kennicutt 2004 for a review about pseudo-bulges). The two galaxies we chose are chosen such that one galaxy, ESO 582-G12, has a flat rotation curve, with a shear, $S = 0.52 \pm 0.05$, in the middle of the range, and the other galaxy,

TABLE 4
GALAXY PARAMETERS USED IN MODEL CONSTRAINTS

Galaxy Name	Distance (Mpc)	h (arcsec)	h (kpc)	B/D	$L_{\rm disk}$ ($\times 10^{10} L_\odot$)	$V_{2.2}$ (km s^{-1})
ESO 582-G12	31.0 ± 0.1	36.5 ± 3.8	5.48 ± 0.57	0.106	1.27 ± 0.11	145
IC 2522	40.3 ± 0.1	20.4 ± 2.1	3.98 ± 0.41	0.164	1.55 ± 0.14	216

NOTES.—Col. (1) galaxy names; col. (2) distances to the galaxies in Mpc, calculated using a Hubble constant $H_0 = 75$ km s^{-1} Mpc^{-1}; col. (3) disk scale lengths, h, in arcseconds; col. (4) disk scale lengths, h, in kpc; col. (5) bulge-to-disk ratio, B/D; col. (6) disk B-band luminosity, $L_{\rm disk}$; col. (7) rotational velocity at 2.2 disk scale length, $V_{2.2}$.

IC 2522, has a continually rising rotation curve, with a shear, $S = 0.39 \pm 0.01$, toward the low end of the range of shears. As a normalization for each galaxy, we take its measured rotation speed at 2.2 disk scale lengths, $V_{2.2}$ (listed in the last column of Table 4), and include a bulge-disk decomposition in order to estimate the baryonic contribution to each rotation curve. In future work we plan to use the same methodology for a large sample of galaxies.

For each of our galaxies we produce surface brightness profiles using the IRAF ellipse routine, which fits ellipses to isophotes in an image, using an iterative method described by Jedrzejewski (1987). From the surface brightness profile we then determine the disk and bulge B-band luminosity using an exponential disk and an exponential (pseudo)bulge. In future papers a more general Sérsic parameterization will be used for the bulge component. We use a one-dimensional bulge-disk decomposition routine, which performs Levenberg-Marquardt least-squares minimization. Explicitly, we fit an exponential profile for each bulge via

$$\mu(R) = \mu_e \exp\{-1.679[(R/R_e) - 1]\}, \qquad (5)$$

where R_e is the effective radius, containing 50% of the total light of the bulge, and μ_e is the surface brightness at R_e. We fit the disk component using

$$\mu(R) = \mu_0 \exp(-R/h), \qquad (6)$$

where μ_0 is the central surface brightness and h is the scale length of the disk. The results of this bulge-disk decomposition can be seen in Figure 4 and Table 4.

We assign masses to the disk and bulge components using a range of stellar mass-to-light ratios from Bell & de Jong (2001). Specifically, in our rotation curve models we allow mass-to-light ratios of $(M/L) = 1.0$, 1.3, and 1.6 (measured in B-band solar units) and use our photometrically derived disk and bulge light profiles $L_B = L_{\rm disk} + L_{\rm bulge}$ to determine the stellar mass contribution to each rotation curve, $M_* = (M/L)L_B$.

We now explore a range of allowed dark matter halo masses and density profiles, adopting two extreme models for disk galaxy formation. In the first we assume that the dark matter halos surrounding these galaxies have not responded significantly to the formation of the disks, i.e., adiabatic contraction (AC) does not occur. We refer to this as our "non-AC" model. In this case, the dark matter contribution to each galaxy rotation curve is described by a density profiles that mirrors those found in dissipationless dark matter simulations,

$$\rho(r) = \frac{\rho_s}{(r/r_s)(1 + r/r_s)^2}, \qquad (7)$$

where r_s is a characteristic "inner" radius, and ρ_s is a corresponding inner density. Here we have adopted the profile shape of Navarro et al. (1996; hereafter NFW). The NFW profile is a two-parameter function and is completely specified by choosing two independent parameters, e.g., the virial mass $M_{\rm vir}$ (or virial radius $R_{\rm vir}$) and concentration $c_{\rm vir} \equiv R_{\rm vir}/r_s$ define the profile completely (see Bullock et al. 2001b for a discussion). Similarly, given a virial mass $M_{\rm vir}$ and the dark matter circular velocity at any radius, the halo concentration $c_{\rm vir}$ is completely determined.

In the second class of models we adopt the scenario of adiabatic contraction (AC) discussed by Blumenthal et al. (1986; see also Bullock et al. 2001a and Pizagno et al. 2005). Here we assume that the baryons and dark matter initially follow an NFW profile and that the baryons cool and settle into the halo center slowly compared to a typical orbital time. This slow infall provokes an adiabatic contraction in the halo density distribution and gives rise to a more concentrated dark matter profile. The idea of adiabatic contraction was originally discussed as to explain the "conspiracy" between dark halos and disk sizes that gives rise to a featureless rotation curve (Rubin et al. 1985) but has since proven to be remarkably accurate in describing the formation of disk galaxies in numerical simulations (e.g., Gnedin et al. 2004, and references therein), although the degree to which this process operates in the real universe is currently uncertain. For example, Dutton et al. (2005) showed that adiabatic contraction models are inconsistent with the rotation curves measured and the expected NFW concentrations for a sample of six galaxies. They suggest that mechanisms such as stellar feedback and stellar bars may result in less concentrated halos than predicted by adiabatic concentration.

In our AC model we take the contraction into account following the prescription of Blumenthal et al. (1986). Note that Gnedin et al. (2004) advocate a slightly modified prescription, but the differences between the two methods are small compared to the differences between our AC model and our non-AC model. In principle, any observational probe that can distinguish between AC- and non-AC-type scenarios provides an important constraint on the nature of gas infall into galaxies (i.e., was it fast or was it slow?).

For each galaxy we iterate over the central and $\pm 1\,\sigma$ values found in the bulge-disk decompositions for h and $L_{\rm disk}$ and explore the three values of mass-to-light ratio discussed above, $(M/L) = 1.0$, 1.3, and 1.6. In each case we assume that M/L remains constant with radius. For each choice of bulge-disk model parameters and mass-to-light ratios, we allow the (initial) halo NFW concentration parameter to vary over the range of viable values, $c_{\rm vir} = 3$–31 (Bullock et al. 2001b). We then determine the halo virial mass $M_{\rm vir}$ necessary to reproduce the value of $V_{2.2}$ for the galaxy and determine the implied fraction of the mass in the system in the form of stars compared to that "expected" from the Universal baryon fraction, $f_* \equiv M_*/(f_b M_{\rm vir})$. We make the (rather loose) demand that f_* lies within the range of plausible values $0.01 f_b < f_* < f_b$.
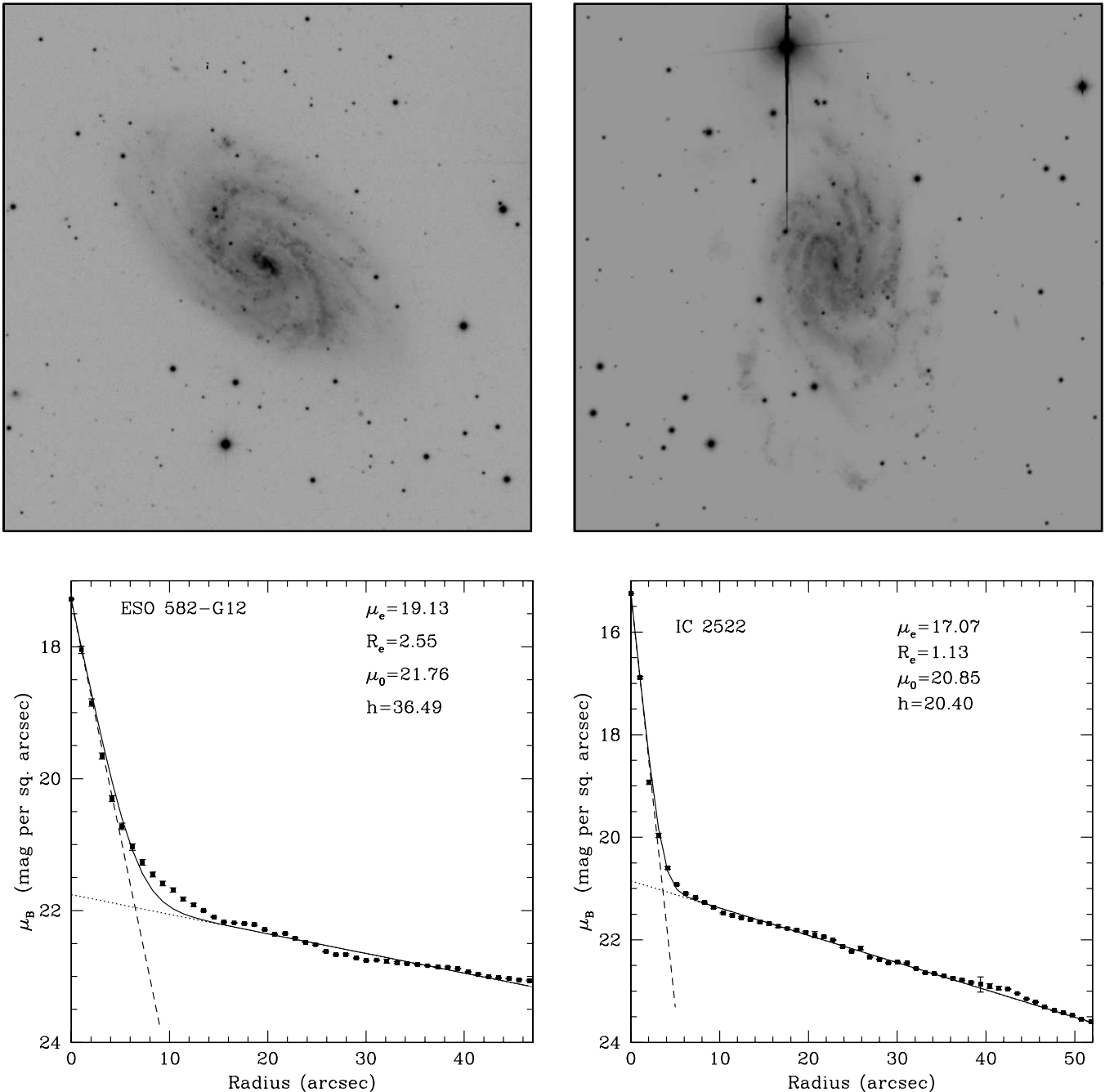
Fig. 4.—Bulge-disk decomposition for two example spiral galaxies as observed in the *B* band. The top row shows a *B*-band image of each galaxy, and the bottom row shows the surface brightness profile and results of the decomposition. The effective radii R_e and disk scale lengths h are measured in arcseconds. The dashed line is the best-fit bulge model, the dotted line is the best-fit disk model, and the solid line is the best combined bulge+disk model. *Left panels*: ESO 582-G12. *Right panels*: IC 2522. The images are aligned such that north is up, and the field is $4.'5 \times 4.'5$.

For each chosen value of $c_{\rm vir}$ and adopted disk formation scenario (AC or non-AC), the chosen $V_{2.2}$ constraint defines the rotation curve completely and thus provides an implied shear rate at every radius. The three panels of Figures 5 and 6 show the results of this exercise for ESO 582-G12 and IC 2522, respectively. In each panel, open symbols are for the non-AC model, and the filled symbols reflect the AC assumption. Each point represents a distinct input combination of h, $L_{\rm disk}$, and M/L. The measured shear rate is illustrated by a solid vertical line, and the $\pm 1\,\sigma$ range in the observe shear rate for each galaxy is shown by the two vertical dashed lines in each panel.

Consider first the left panel of Figure 5. Here we plot the dark matter halo concentration parameter versus the shear rate mea-

sured at 10 kpc. More concentrated halos generally produce higher shear rates, as expected. It can be seen that for a given NFW concentration, $c_{\rm vir}$, several values of shear are possible. This is due to changes in the baryon contribution (i.e., the disk mass and disk scale length) to the rotation curve. Whether an increase in the baryon contribution causes the shear to increase or decrease depends on the size of the disk (i.e., the disk scale length). The same is true for Figure 6. In the AC model (*filled circles*), $c_{\rm vir}$ refers to the halo concentration *before* the halo is adiabatically contracted. This is why the AC points tend to have higher shear values at fixed $c_{\rm vir}$ compared to the non-AC case. Every point (or h, $L_{\rm disk}$, M/L input combination) has an associated stellar baryon fraction f_* and dark halo virial mass $M_{\rm vir}$. These values are
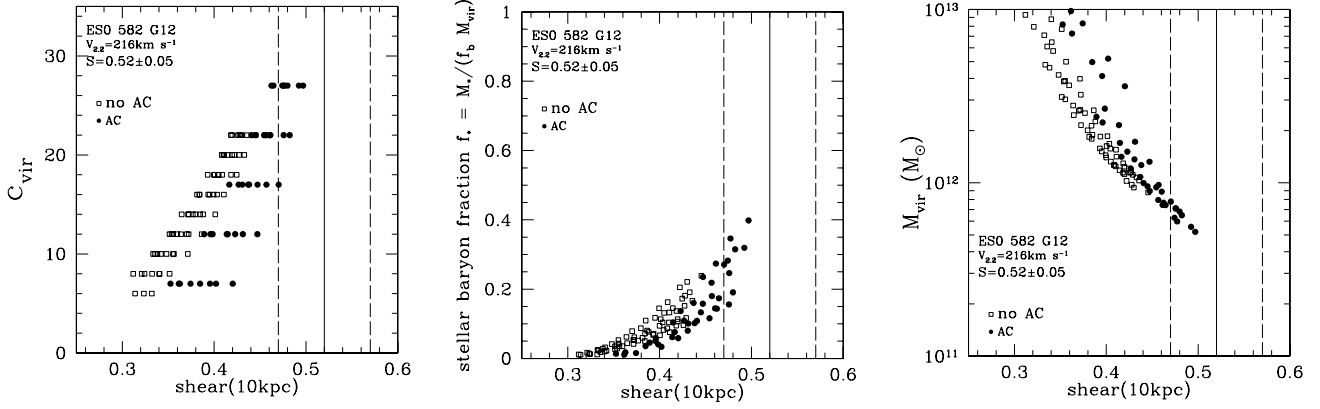
Fig. 5.—Model results for ESO 582-G12. *Left*: NFW concentration vs. shear; *center*: stellar baryon fraction vs. shear; *right*: virial mass vs. shear. The open squares represent the model without an adiabatically contracted dark matter halo (non-AC), and the filled circles represent the model with adiabatic contraction (AC). The vertical lines present the measured shear (*solid line*) with the 1 σ error added and subtracted (*dashed lines*).

plotted versus shear rate in the middle and right panels in Figure 5. Observe that with only the $V_{2.2}$ constraint imposed (all points), a wide range of dark matter halo properties are allowed. Once we constrain the models by forcing the predicted shear to be consistent the observed range $S = 0.47$–0.57, we favor models that include adiabatic contraction. The dark matter of halo of ESO 582-G12 is constrained to be of relatively low mass, $M_{vir} \simeq (5-8) \times 10^{11} \, M_{\odot}$, and to have a fairly high NFW concentration, $c_{vir} > \sim 16$. This is consistent with the high end of the c_{vir} distribution predicted for LCDM (Bullock et al. 2001b). The stellar mass in the galaxy is between $\sim 15\%$ and 40% of the baryonic mass associated with its dark matter halo.

Figure 6 shows analogous results for IC 2522. Unlike ESO 582-G12, this galaxy prefers a more massive, low-concentration halo, $M_{vir} \simeq (1.5-6) \times 10^{12} \, M_{\odot}$ with $c_{vir} \simeq 2 - 8$, at the low end of the c_{vir} distribution (Bullock et al. 2001b). The implied stellar mass is quite small; $<10\%$ of the universal baryon budget has ended up on stars. Furthermore, the measured shear rate of this galaxy favors our non-AC model. This is in qualitative agreement with results presented by Dutton et al. (2005).

Model results for the central mass concentration in each galaxy are shown in Figures 7 and 8. Here c_{tot} and c_{dm} correspond to the fraction of the total and dark matter mass contained within central 10 kpc of each system. We see that ESO 582-G12 contains roughly 20% of its mass within 10 kpc, while IC 2552 is quite diffuse, with $c_{tot} < 5\%$.

What drives these differences? Take IC 2522 for example, which has a very low concentration. This arises because of the

combination of its (small) disk scale length *and* the fact that the rotation curve is rising at 10 kpc (implied by a shear of 0.39 ± 0.1). The rotation curve of the stellar disk alone peaks at 2.2 scale lengths (~ 8.8 kpc) and will be falling at 10 kpc (where the shear is measured). The measured shear of 0.39 ± 0.01 at 10 kpc implies that the total rotation curve is rising at 10 kpc, which means the dark matter must be very extended (or of low concentration). ESO 582-G12, on the other hand, has a falling rotation curve at 10 kpc but a *larger* disk scale length. This requires a more concentrated halo to explain the observed shear rate.

The two galaxies chosen for this modeling are, in many ways, quite comparable. Their Hubble types, B/D ratios, and disk luminosities are very similar. The only significant difference is in their measured rates of shear. The differences in their favored formation models (AC for ESO 582-G12 versus non-AC for IC 2522), halo masses, and concentrations, come down to a different measurement for their shear and the sizes of their disks. It is quite interesting that two galaxies that seem so similar in size and Hubble type seem to inhabit very different types of dark matter halos. It is tempting to speculate that the shear rate itself provides an underlying physical driver to push galaxies in drastically different dark matter halos toward similar luminosities. However, the problem would then be what stops such a drive and makes the galaxy luminosities so similar, when the halo masses show large differences.

This clearly demonstrates that the shear rate adds an important constraint on galaxy formation models compared to what can be learned from standard Tully-Fisher constraints alone. Indeed, the results for IC 2522 and ESO 582-G12 are tantalizing. The first,
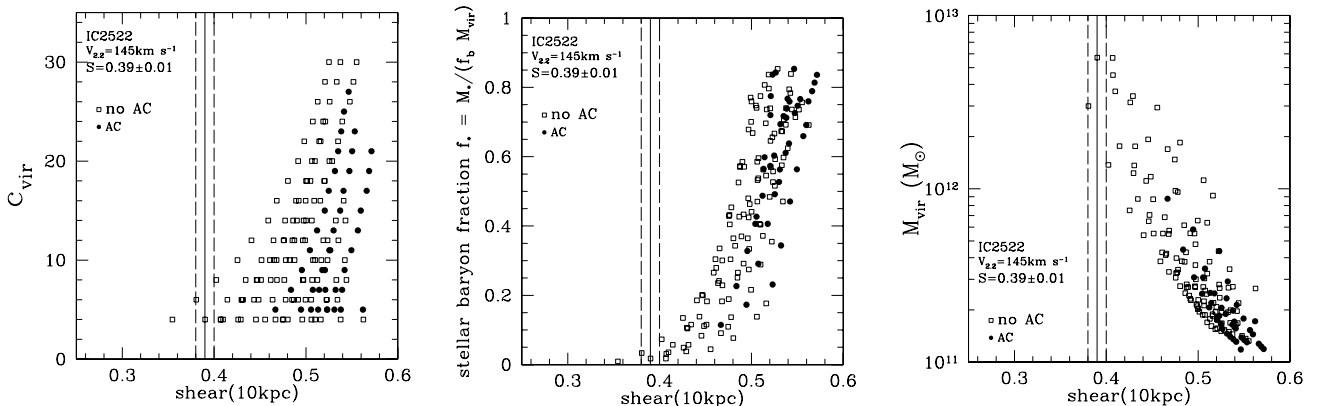

Fig. 6.—Model results for IC 2522. *Left*: NFW concentration vs. shear; *center*: stellar baryon fraction vs. shear; *right*: virial mass vs. shear. The open squares represent the model without an adiabatically contracted dark matter halo (non-AC), and the filled circles represent the model with adiabatic contraction (AC). The vertical lines present the measured shear (*solid line*) with the 1 σ error added and subtracted (*dashed lines*).
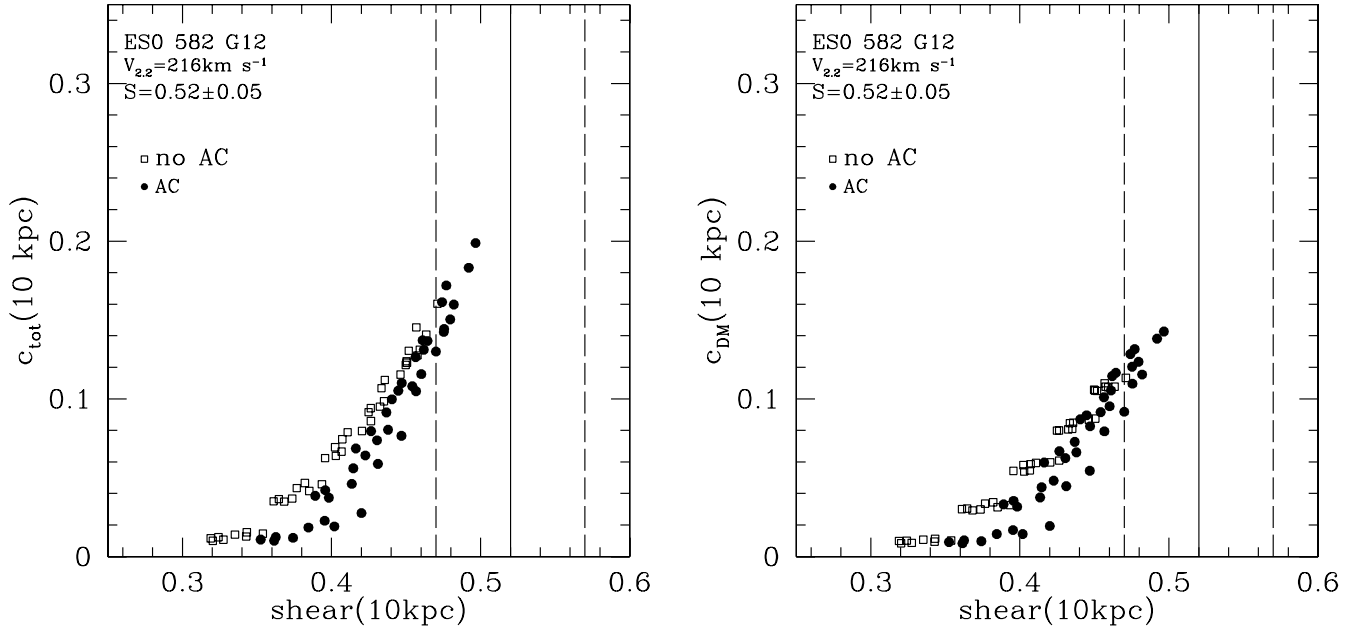
FIG. 7.—Model results for ESO 582-G12. *Left*: Central mass concentration (mass fraction within 10 kpc) vs. shear; *right*: dark matter concentration (dark matter mass fraction within 10 kpc) vs. shear. The open squares represent the model without adiabatic contraction of the stellar halo, and filled circles represent the model with adiabatic contraction. The vertical lines present the measured shear (*solid line*) with the 1 σ error added and subtracted (*dashed lines*).

with a low shear rate, favors a nonadiabatically contracted halo with a low halo concentration and a massive, extended dark matter halo. The second, with a high shear rate, favors an adiabatically contracted halo with a high NFW concentration and relatively low virial mass. These two cases motivate the application of the shear rate constraint to a larger sample of galaxies. Since shear is related to the spiral arm pitch angle and spiral arms are clearly detectable in disk galaxies at $z \sim 1$ (e.g., Elmegreen et al. 2004), it is possible to constrain models of disk formation and dark matter halo structure back to a look-back time of ~ 7 Gyr and evaluate how the mass distribution in disk galaxies changes with time.

An important test of our modeling is how well the modeled rotation curves fit the data. Figure 9 shows the observed rotation curves from Persic & Salucci (1995) overlaid with our modeled rotation curves. In both cases the rotation curve is modeled well in the outer parts, where we are measuring the shear. In the inner regions, where the bulge is important, both rotation curve models overestimate the observed rotation curve, although the model for ESO 582-G12 presents a much better case than that for IC 2522. For IC 2522 the solid line represents a model rotation curve, with a bulge-to-disk ratio of 0.164 (see Table 4) and a bulge effective radius of 0.2 kpc (as measured in the one-dimensional decomposition). However, infrared imaging of IC 2522 (see Fig. 10)
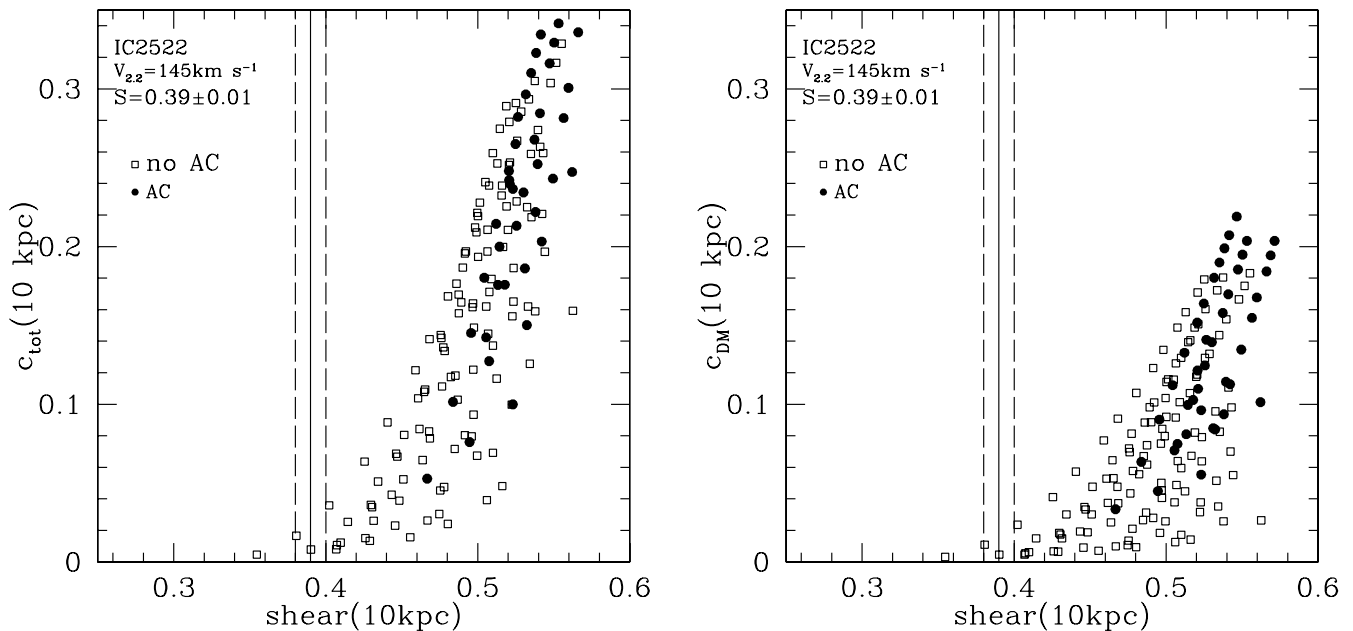

FIG. 8.—Model results for IC 2522. *Left*: Central mass concentration (mass fraction within 10 kpc) vs. shear; *right*: dark matter concentration (dark matter mass fraction within 10 kpc) vs. shear. The open squares represent the model without adiabatic contraction of the stellar halo, and filled circles represent the model with adiabatic contraction. The vertical lines present the measured shear (*solid line*) with the 1 σ error added and subtracted (*dashed lines*).
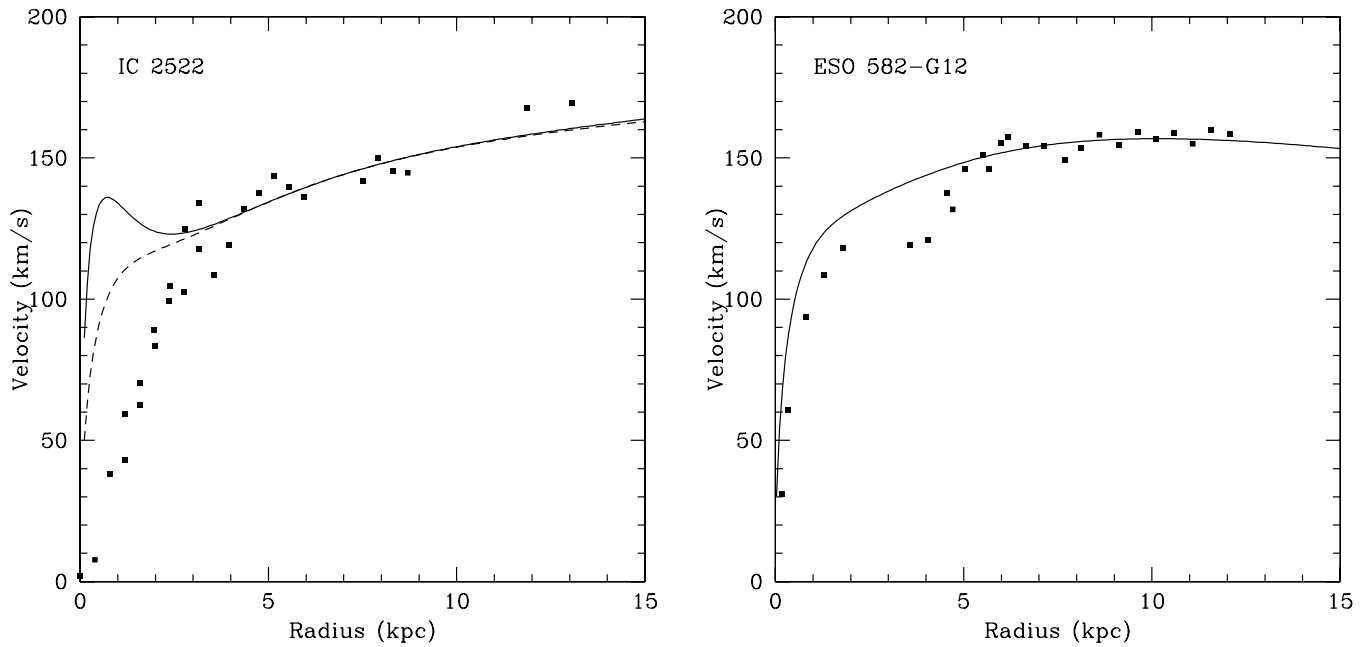
Fig. 9.—Observed rotation curves with the overlaid model rotation curves for IC 2522 (*left*) and ESO 582-G12 (*right*). The errors on the data points are typically <10% (Persic & Salucci 1995). The solid lines represent the rotation curve that best matches the observed shear at 10 kpc. For IC 2522 the dashed line represents a model rotation curve with a bulge that has an effective radius that is a factor of 2 larger than measured in the one-dimensional decomposition, in order to mimic the effect of a bar with a major-to-minor axis ratio of ~2.

reveals that this galaxy has a bar with a major axis length ~2 kpc (i.e., the radius within which the model overestimates the observed rotational velocities) and a major to minor axis ratio of ~2. (It is common for near-IR imaging to reveal bars that may have been hidden due to dust extinction in an optical image, e.g., Seigar & James 1998a; Eskridge et al. 2000; Seigar 2002; Seigar et al. 2003.) The spectroscopic data taken by Mathewson et al. (1992) were observed with a slit aligned along the major axis of each galaxy, and in the case of IC 2522, the major axis of the bar is well aligned with the galaxy major axis. The stellar orbits

Fig. 10.—K_s-band image of IC 2522, revealing a bar that was not evident in the optical imaging of this galaxy. The image is aligned such that north is up, and the field is 3.′3 × 3.′3.

within a bar are such that the dominant motion is parallel to its major axis (e.g., Athanassoula 1992), and so this will account (to some extent) for the low values of the measured rotation velocities (compared to the modeled values) within a few kpc. Furthermore, if we double the effective radius of the modeled bulge, the resulting rotation curve is the dashed line in Figure 9. This still fits the outer part of the galaxy rotation curve extremely well, and the central velocities are not as badly overestimated. Modifying the mass models in this way does not affect the trends displayed in Figures 6 and 8, it just affects how well the model reproduces the inner part of the observed rotation curve. This is probably because the main constraints we are using to model these galaxies are at a 10 kpc radius, well outside the region where the bulge or bar is dominating the rotational velocities. As a result the concentrations we determine from our modeling do not depend on the mass distribution assumed for the bulge (i.e., the mass distribution within the central few kpc). This approach is therefore a powerful and robust method, because its constraints are relatively insensitive to the details of bars versus bulges in the central regions.

6. CONCLUSIONS

In this paper we have shown that near-infrared and optical spiral arm pitch angles are the same on average, and as a result we have strengthened the correlation between spiral arm pitch angle and shear rate originally shown in Seigar et al. (2005) and expanded here using optical data. Using an infall model, we have shown that the use of rates of shear (which can now be derived from spiral arm pitch angles) allow us to put constraints on the total central mass concentration, the dark matter concentration, and the initial NFW concentration. In some cases it may be possible to determine if the infall must occur adiabatically or nonadiabatically, and this is demonstrated by IC 2522, which must undergo nonadiabatic infall.

This method can be used to determine the central concentrations of galaxies and to constrain galaxy formation models in any
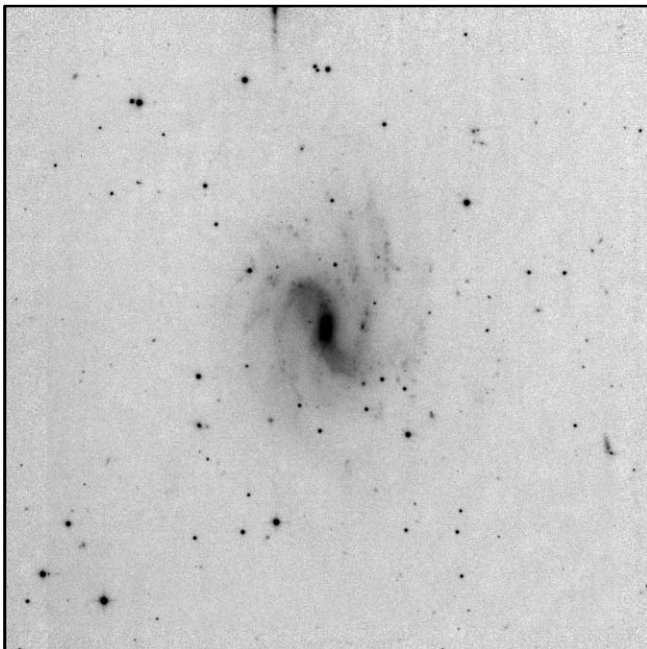
galaxy that has detectable spiral structure. In future papers we will apply our technique to a large sample of galaxies. Furthermore, since spiral structure can clearly be seen in disk galaxies out to $z \sim 1$ (Elmegreen et al. 2004), the evolution of central mass concentrations in disk galaxies can be estimated as a function of look-back time, and we plan to investigate this as well.

REFERENCES

Athanassoula, E. 1992, MNRAS, 259, 328
Bell, E. F., & de Jong, R. S. 2001, ApJ, 550, 212
Bertin, G. 1991, in Proc. IAU Symp 146, Dynamics of Galaxies and Their Molecular Cloud Distributions, ed. F. Combes, & F. Casoli (Dordrecht: Kluwer), 93
———. 1993, PASP, 105, 640
———. 1996, In New Extragalactic Perspectives in the New South Africa, ed. D. L. Block, & J. M. Greenberg (Dordrecht: Kluwer), 227
Bertin, G., & Lin, C. C. 1996, Spiral Structure in Galaxies: A Density Wave Theory (Cambridge: MIT Press)
Bertin, G., Lin, C. C., Lowe, S. A., & Thurstans, R. P. 1989a, ApJ, 338, 78
———. 1989b, ApJ, 338, 104
Block, D. L., Bertin, G., Stockton, A., Grosbol, P., Moorwood, A. F. M., & Peletier, R. F. 1994, A&A, 288, 365
Block, D. L., & Puerari, I. 1999, A&A, 342, 627
Block, D. L., Puerari, I, Frogel, J. A., Eskridge, P. B., Stockton, A., & Fuchs, B. 1999, Ap&SS, 269, 5
Block, D. L., & Wainscoat, R. 1991, Nature, 353, 48
Blumenthal, G. R., Faber, S. M., Flores, R., & Primack, J. R. 1986, ApJ, 301, 27
Bullock, J. S., Dekel, A., Kolatt, T. S., Kravtsov, A. V., Klypin, A. A., Porciani, C., & Primack, J. R. 2001a, ApJ, 555, 240
Bullock, J. S., Kolatt, T. S., Sigad, Y., Somerville, R. S., Kravtsov, A. V., Klypin, A. A., Primack, J. R., & Dekel, A. 2001b, MNRAS, 321, 559
Burstein, D., & Rubin, V. C. 1985, ApJ, 297, 423
Considère, S., & Athanassoula, E. 1988, A&AS, 76, 365
de Jong, R. S. 1996, A&A, 313, 45
de Vaucouleurs, G., de Vaucouleurs, A., Corwin, H. G., Jr., Buta, R. J., Paturel, G., & Fouqué, R. 1991, The Third Reference Catalog of Bright Galaxies (New York: Springer) (RC3)
Dutton, A. A., Courteau, S., de Jong, R., & Carignan, C. 2005, ApJ, 619, 218
Elmegreen, B. G., Elmegreen, D. M., & Hirst, A. C. 2004, ApJ, 612, 191
Eskridge, P. B., et al. 2000, AJ, 119, 536
———. 2002, ApJS, 143, 73
Fall, S. M., & Efstathiou, G. 1980, MNRAS, 193, 189
Fuchs, B. 1991, in Dynamics of Disk Galaxies, ed. B. Sundelius (Göteberg: Chalmers Univ. Tech.), 359
———. 2000, in ASP Conf. Ser. 197, Dynamics of Galaxies, ed. F. Combes, G. A. Mamon, & V. Charmandaris (San Francisco: ASP), 53

Garcia-Gomez, C., & Athanassoula, E. 1993, A&AS, 100, 431
Gnedin, O. Y., Kravtsov, A. V., Klypin, A. A., & Nagai, D. 2004, ApJ, 616, 16
Goldreich, P., & Lynden-Bell, D. 1965, MNRAS, 130, 125
Gonzalez, R. A., & Graham, J. R. 1996, ApJ, 460, 651
Grosbol, P. J., & Patsis, P. A. 1998, A&A, 336, 840
Grosbol, P., Patsis, P. A., & Pompei, E. 2004, A&A, 423, 849
Hubble, E. P. 1926, ApJ, 64, 321
Jedrzejewski, R. I. 1987, MNRAS, 226, 747
Julian, W. H., & Toomre, A. 1966, ApJ, 146, 810
Kennicutt, R. C. 1981, AJ, 86, 1847
Kormendy, J., & Kennicutt, R. C. 2004, ARA&A, 42, 603
Lin, C. C., & Shu, F. H. 1964, ApJ, 140, 646
Mathewson, D. S., Ford, V. L., & Bucchorn, M. 1992, ApJS, 81, 413
Navarro, J. F., Frenk, C. S., & White, S. D. M. 1996, ApJ, 462, 563 (NFW)
Persic, M., & Salucci, P. 1995, ApJS, 99, 501
Pizagno, J., et al. 2005, ApJ, 633, 844
Rhoads, J. E. 1998, AJ, 115, 472
Rubin, V. C., Burstein, D., Ford, W. K., & Thonnard, N. 1985, ApJ, 289, 81
Schröder, M. F. S., Pastoriza, M. G., Kepler, S. O., & Puerari, I. 1994, A&AS, 108, 41
Seigar, M. S. 2002, A&A, 393, 499
———. 2005, MNRAS, 361, L20
Seigar, M. S., Block, D. L., & Puerari, I. 2004, in Penetrating Bars through Masks of Cosmic Dust, ed. D. L. Block et al. (Dordrecht: Springer), 155
Seigar, M. S., Block, D. L., Puerari, I., Chorney, N. E., & James, P. A. 2005, MNRAS, 359, 1065
Seigar, M. S., Chorney, N. E., & James, P. A. 2003, MNRAS, 342, 1
Seigar, M. S., & James, P. A. 1998a, MNRAS, 299, 672
———. 1998b, MNRAS, 299, 685
Thornley, M. D. 1996, ApJ, 469, L45
Toomre, A. 1981, in The Structure and Evolution of Normal Galaxies, ed. S. M. Fall, & D. Lynden-Bell (Cambridge: Cambridge Univ. Press), 111
Tully, R. B., & Fisher, J. R. 1977, A&A, 54, 661
Worthey, G. 1994, ApJS, 95, 107